Desalination and Water Treatment
www.deswater.com

doi: 10.5004/dwt.2023.29630

298 (2023) 184–198
June

Hydroxyapatite/superparamagnetic iron oxide nanoparticles nanocomposite for Congo red adsorption

Do Thi Hai[a], Nguyen Thu Phuong[b,*], Pham Xuan Cong[c], Nguyen Hong Nam[c], Le Phuong Thu[c], Nguyen Thi Thu Trang[b], Nguyen Thi Thom[b], Pham Thi Nam[b], Magdalena Osial[d], Dinh Thi Mai Thanh[b,c,*]

[a]*Faculty of Basic Science, Hanoi University of Mining and Geology, 18 Pho Vien, Duc Thang, Nam Tu Liem, Hanoi, Vietnam, Tel.: 0084985711428; email: dothihai.71@gmail.com (D.T. Hai)*
[b]*Institute for Tropical Technology, Vietnam Academy of Science and Technology, 18 Hoang Quoc Viet, Cau Giay, Hanoi 10000, Vietnam, Tel.: 0084982924405; email: ntphuong@itt.vast.vn (N.T. Phuong), Tel.: 0084904409452; ntttrang@itt.vast.vn (N.T.T. Trang), Tel.: 0084973197326; email: ntthom@itt.vast.vn (N.T. Thom), Tel.: 0084983499058; email: ptnam@itt.vast.vn (P.T. Nam)*
[c]*University of Science and Technology of Hanoi, Vietnam Academy of Science and Technology, 18 Hoang Quoc Viet, Cau Giay, Hanoi 10000, Vietnam, Tel.: 0084914256885; email: dinh-thi-mai.thanh@usth.edu.vn (D.T.M. Thanh), Tel.: 0084327067338; email: congpx.ba9009@st.usth.edu.vn (P.X. Cong), Tel.: 0084967720086; email: nguyen-hong.nam@usth.edu.vn (N.H. Nam), Tel.: 0084392411761; email: le-phuong.thu@usth.edu.vn (L.P. Thu)*
[d]*Department of Theory of Continuous Media and Nanostructures, Institute of the Fundamental Technological Research, Polish Academy of Sciences, Pawińskiego 5B Str., 02-106 Warsaw, Poland, Tel.: 0048228261281; email: mosial@ippt.pan.pl (M. Osial)*

Received 5 October 2022; Accepted 22 May 2023

ABSTRACT

In this work, a nanostructural composite based on the superparamagnetic iron oxide nanoparticles (SPIONs) coated with hydroxyapatite (HAp) was demonstrated as an effective adsorbent for the removal of the Congo red (CR) from aqueous solutions. Prior to its application on the model pollutant, the morphology, crystallinity, specific surface area, chemical composition, and magnetic properties were characterized with several techniques, including scanning electron microscopy, transmission electron microscopy, Fourier-transform infrared spectroscopy, X-ray diffraction, Brunauer–Emmett–Teller, and vibrating sample magnetometer. Amongst composites synthesized in different ratios of SPION's weight, the composite containing 35 wt.% of SPION was chosen to adsorb CR. The magnetization saturation of the latter was about 20.39 emu·g^{-1}, still enough for magnetic separation. The effect of adsorbent mass, pH, initial concentration, temperature, and contact time on the adsorption efficiency and capacity of CR was evaluated using UV-Vis spectrometry. It was shown that the most effective results of CR removal were achieved for 0.10 g dosage of SPION/HAp to absorb 50 mL of CR solution of 50 mg·L^{-1} at pH_0 and a contact time of 4 h. The CR adsorption process on SPION/HAp composite is matched with the pseudo-second-order kinetic model and the Langmuir model. The obtained thermodynamic parameters ($\Delta G° > 0$, $\Delta H° = -39.02$ kJ·mol^{-1}, $\Delta S° = -0.134$ kJ·mol^{-1}·K^{-1}) suggest that the adsorption of CR onto the composite is non-spontaneous, exothermic, with a rising of randomness at the adsorbate–adsorbent interface. The maximum CR adsorption capacity using the SPION/HAp adsorbent was determined to be 158.98 mg·g^{-1}, suggesting that the adsorbent has a satisfactory potential to adsorb CR. The chosen composite can be easily separated using magnets, making it a promising material for wastewater treatment.

Keywords: Superparamagnetic iron oxide nanoparticles/hydroxyapatite (SPION/HAp); Magnetic nanoparticles; Apatite ore; Adsorption; Congo red; Wastewater treatment

* Corresponding authors.

1. Introduction

Organic dyes, including both cationic and anionic dyes, have been widely employed in numerous areas over the last century, including textiles, paper, printing, plastic, rubber, coating, leather, and the food industry [1]. Thanks to the acceleration of modernization and industrialization, the entire number of natural and synthetic dyes on the market has surpassed 10,000, and global annual output has already exceeded 7×10^5 million tons [2]. However, around 5% to 10% of these dyes are discharged into the aquatic environment without treatment and contributed to 20% of water pollution [3]. Many dyes are difficult to treat within the photo- and bio-degradation, so other ways of their removal from water are deeply needed [4].

Congo red [1-naphthalene sulfonic acid, 3,30-(4,40-biphenylenebis (azo)) bis(4-amino-)disodium salt, CR] is a benzidine-based anionic diazo dye with pK_a of 4.5 which has two azo groups [5,6]. It forms a red colloidal solution in water, where it is expected to metabolize to benzidine, a chemical that has been linked to carcinogenic and mutagenesis effects in aquatic animals [7,8]. Its increased content in drinking water comes from the textile and chemical industries, textile dyeing, paper, cosmetics, and even rubber or pharmaceutical industry [9–12] making it a pollutant causing severe health effects [13]. Some studies also refer to its adverse effect on the eyes, and skin, and relate it to respiratory problems [14]. CR has been outlawed in many nations due to health risks but is otherwise regularly consumed in many other countries [15]. Basically, even a tiny amount of dye discharge into water resources inhibits its light penetration and alters the gas solubility for photosynthesis and respiration activities [4]. Directing touch with dissolved dyes might irritate eyes and skin [16]. Therefore, wastewater containing dyes like CR must be purified before being released into an aquatic environment [17,18].

Literature refers to many ways to remove CR from water and wastewater, including oxidation [19], ozonation [20], electrochemical process [21], electro-Fenton process [22], Fenton-biological treatment [23], enzymatic treatment [24], membrane filtration [25], photocatalytic degradation [26], biological treatment [27], biological degradation [28], and adsorption [8]. Despite the high effectiveness of some techniques, water purification still is challenging. For example, biological treatment is slow in achieving the desired removal state. Membrane separation and oxidation generate secondary waste, and the cost of operation is high, making them non-cost effective. Among different techniques, adsorption is broadly recognized as the most efficient technique for reducing dye effluent, even at low concentrations. Such water pollution treatment technique is also cost-effective, facile to scale up, and simple in operation, while its effectiveness depends on the type of adsorbent.

Due to high adsorption capacity, small particle size, large surface area, high catalytic activity, and thermal stability, nanomaterials have received a lot of attention in recent years to be used in wastewater treatment with the adsorption of pollutants [29]. So far, many non-conventional adsorbents such as bentonite [30], montmorillonite [31], coir pith carbon [32], mesoporous activated carbons [33], fly ash [34], activated red mud [34], rice hull ash [35], leaf [36], rice husk [37], chitosan [38], and hydroxyapatite (HAp) [39] have been used to treat CR from aqueous solutions. Especially the last material, HAp, offers effective water purification. It is an eco-friendly mineral that naturally occurs in bones and teeth, and it can easily be synthesized artificially [40]. For its high porosity and large surface area, it can adsorb a variety of inorganic and organic substances, including organic pollutants and inorganic salts. Literature refers its promising use over Methylene blue, methyl orange, phenol red, phenol [41], Congo red [39], nitrobenzene [42], F^-, antibiotic [43], Co^{2+}, Ni^{2+}, Hg^{2+}, Fe^{3+} [44], Cr(VI) [45], Ag^+ [46], Cu^{2+}, Zn^{2+}, Cd^{2+} [47] revealing its large adsorption capacity, biodegradability, inexpensiveness, stability, and reactivity [48]. HAp can be easily synthesized from many sources, including apatite ore. One of the tremendous resources of apatite offering over 2,550 tons is in Vietnam, Lao Cai province, making HAp cost-effective to be synthesized during the facile modification of ores. Nanostructural HAp made from apatite offers adsorption efficiency in the range of 83.7% to 99.9%, and the adsorption capacity for F^- is from 2.74 to 7.2 $mg \cdot g^{-1}$ [49], for Pb^{2+} from 7.94 to 14.3 $mg \cdot g^{-1}$, for Zn^{2+} is from 19.26 $mg \cdot g^{-1}$ [50], for Cd^{2+} from 103–122 $mg \cdot g^{-1}$ [51].

Another promising adsorbent is based on the superparamagnetic iron oxide nanoparticles (SPIONs) having a core mainly made of γ-Fe_2O_3 (maghemite) or Fe_3O_4 (magnetite) particles with sizes below 35 nm [52]. SPIONs can be easily synthesized and offer a high volume-to-surface ratio and fast attraction by magnets. These properties along with non-cytotoxicity [53,54], and facile doping, or surface modification [55,56] make it a multifunctional material for the adsorption of pollutants from aqueous media and magnetic separation, maintaining a low cost of its synthesis and operation [57]. Due to their simplicity in production and their non-toxic characteristic, magnetite (Fe_3O_4) nanoparticles have attracted the most attention among the advanced magnetic nanoparticles, despite their agglomeration and instability in highly oxidizing and acidic environments [58]. The drawback is the ability of iron oxide molecules in a solution to interact with one another through hydrophobic interactions and aggregate into larger groups of particles with smaller, poorer surface areas. Additionally, because they have a lower bonding potential than hydrated ferric oxide, they have a lower capacity for adsorbing pollutants, necessitating surface modification and functionalization with several compounds, including silica, fatty acids, chitosan, polyethylene glycol, and apatite, to prevent their surface from acidic media [59].

SPIONs and their composites like SPION/HAp can be easily separated from the purified water within a magnetic field without filtration or centrifugation, reducing the amount of waste that is released into the environment [60]. Literature refers successful application of SPION/HAp composites to treat water pollutants like Methylene blue [61] or heavy metal ions [62], where the HAp was made from chicken bones. As follows, HAp was also made from eggshells to be used as SPION/HAp composite for Methylene blue treatment [63]. Despite the effectiveness of the proposed composite, the modification from animal sources for HAp production required the application of high temperatures, generating expensive costs. Therefore, in this work, the composite based on SPION and HAp, where

the HAp was made from apatite ore, was proposed as an inexpensive adsorbent that can be used for the magnetic separation of dye pollutants from water. SPION/HAp was synthesized by the co-precipitation method delivering the material with a high surface area. It was used to remove Congo red (CR) in the function of contact time, initial CR concentration, pH, adsorbent mass, and temperature on adsorption capacity and efficiency.

2. Materials and methods

2.1. Materials chemicals

The apatite ore is collected from Lao Cai Province, Vietnam. HNO_3 65%–68%, citric acid $HOC(CH_2CO_2H)_3$ 99.5%, sodium hydroxide NaOH 96%, ammonia NH_3 25%–28%, Congo red ($C_{32}H_{22}N_6Na_2O_6S_2$) are pure chemicals from Anh Tuan Chemical Company Limited, Vietnam. Iron chloride tetrahydrate $FeCl_2{\cdot}4H_2O$ 98%, and iron chloride hexahydrate $FeCl_3{\cdot}6H_2O$ 99% are pure chemicals of Merck. Acetone $(CH_3)_2CO$ 99% is a pure chemical from Xilong, China.

2.1.1. Apatite modification experiment

The pristine apatite ore was ground and dried at 100°C. Then, 1 g of ore was treated with 20 mL of 1 M HNO_3 and stirred at a rate of 400 rpm for 30 min to dissolve. With this procedure, 20 mL of precursor for the synthesis of 0.5 g of HAp was obtained. The increase in the mass of ore requires an increase in the volume of HNO_3 for scaling up. After stirring, the solution was filtered to separate insoluble substances.

2.1.2. Fe_3O_4 synthesis

0.1992 g $FeCl_2{\cdot}4H_2O$ was added to 0.5413 g $FeCl_3{\cdot}6H_2O$ dissolved in 10 mL distilled water under a nitrogen atmosphere in a 50 mL glass bottle. In a fume hood, 20–25 mL of NH_3 was added dropwise to reach pH 10–11. After 30 min of stirring at 80°C and 1,300 rpm, the precipitate was decanted on a magnet and washed with distilled water until it reached a pH of 7, yielding 0.2 g SPION.

2.1.3. Fe_3O_4 modified

Wet precipitate containing 0.2 g of Fe_3O_4 was filled with 50 mL sodium citrate solution pH 5.5 (made from 0.1 M citric acid, where NaOH was added to adjust particular pH) and stirred at 1100 rpm for the first 30 min at 60°C and 600 rpm for the second 30 min. Finally, the product was decanted magnetically and cleaned three times with 2 mL acetone. Then, the SPION modified with citrates was suspended in distilled water.

2.1.4. Fe_3O_4/HAp synthesis

Following previous studies, from 20 mL ore solution, after the precipitation process by NH_3 solution, 0.5 g HAp was obtained. In order to synthesize the composite with different ratios, various volumes of ore solution were used with 0.2 g of SPION. NH_3 and ore solution were added dropwise to ensure a pH of 10 for the solution. After 30 min of stirring at 800 rpm, the product was collected at the bottom of the container onto the magnet and washed with water until pH 7. Finally, the material was dried and ground, yielding SPION/HAp.

2.2. Congo red adsorption experiments

The Congo red adsorption experiments were conducted with 50 mL solution in the range of concentration from 25 to 900 mg·L^{-1}. A mass of SPION/HAp (from 0.01 g to 0.15 g) was immersed into the solution. Initial pH values of the solution were adjusted from 4 to 12 using 0.01 M NaOH and 0.01 M HCl and a pH meter was used to check the pH solution. By using a shaker at a rate of 250 rpm, the mixtures were stirred at various times (0.5, 1, 2, 3, 4, 5, and 6 h).

CR adsorption efficiency H (%) and capacity Q (mg·g^{-1}) were determined by the following equations:

$$H = \left(C_0 - C_e\right) \times \frac{100}{C_0} \tag{1}$$

$$Q = \left(C_0 - C_e\right) \times \frac{V}{m} \tag{2}$$

where C_0 (mg·L^{-1}) is the initial CR concentration in the solution, C_e (mg·L^{-1}) is the equilibrium CR concentration after the adsorption process, V (L) is the solution volume (V = 50 mL), and m (g) is the mass of SPION/HAp.

2.3. Methods

SPION/HAp composite was characterized by the saturation magnetization, the molecular structure, phase component, morphology, specific surface area, and element component by a vibrating sample magnetometer (home-made VSM) at room temperature with the maximum applied field of 11 kOe, infrared (IR, Nicolet iS10, Thermo Scientific), scanning electron microscope-energy-dispersive X-ray spectroscopy (SEM-EDS, Hitachi S-4800-Japan), X-ray diffraction (XRD, D8 ADVANCE-Bruker, CuK_α radiation (λ = 1.54056 Å) with a step angle of 0.030°, scanning rate of 0.04285°s^{-1}, and 2θ degree in the range of 20°–70°), Brunauer–Emmett–Teller method (BET, TriStar II, Micromerit, 77K, N_2).

The CR concentrations were determined by the UV-Vis method at a wavelength of 497 nm on a UV-Vis Spectrometer S80 Libra (Biochrom, UK).

3. Results and discussion

3.1. Characterization of SPION/HAp

3.1.1. Fourier-transform infrared spectroscopy and XRD analysis

Initially, the chemical composition of the obtained composite was investigated based on the Fourier-transform infrared spectroscopy (FT-IR) analysis, and the presence of particular, characteristic bands corresponding to the presence of SPIONs and HAp in the SPION/HAp nanocomposite were recorded. Studies were performed for the nanocomposite having different stoichiometry from pristine SPIONs to a composite containing 40% of wt% of

SPIONs. As can be seen in Fig. 1, the peak at 619.96 cm^{-1} corresponds to the Fe–O bond of magnetite [64] confirming the presence of iron oxide in the samples. An increase of HAp in the composite leads to the shift of this band to 587.24 cm^{-1}. For composites, the band at 1,050.73 cm^{-1} is related to PO_4^{3-} bands, which is in good agreement with the literature [65]. An observed peak in the range of 3,432.23 and 3,435.64 cm^{-1}, respectively, in the FT-IR analysis of Fe_3O_4 and Fe_3O_4/HAp nanocomposites, is attributed to the stretching vibrations of the OH^- groups or the absorbed water [66]. Furthermore, the bending vibration of the OH^- group is also characterized by a peak at a wavenumber of 1,628.04 cm^{-1}. The peak at 1,394.26 cm^{-1} corresponds to the NO_3^- group because HNO_3 is used to dissolve apatite ore in the composite synthesis process [67].

Complementary to the FT-IR analysis, the XRD method was also used for the characterization of the composite. According to Fig. 2, the XRD patterns demonstrate the existence of Fe_3O_4 and HAp, where the HAp phase is marked with the * symbol, and iron oxide with the + symbol. The cubic structure of pure Fe_3O_4 nanoparticles is described by diffraction peaks with 2θ at 35.65°, 43.24°, 57.31°, and 62.91°, which are assigned to the corresponding (311), (511), (222), and (004) crystal planes (the JCPDS No. 19-0629) [64]. The formation of the HAp phase is suggested by the diffraction angles of 25.97°, 32.1°, 39.8°, 46.92°, and 49.6°, which are attributed to (002), (211), (310), (222), and (004), respectively (COD No. 96-900-2215) [68]. When the ratio of Fe_3O_4 in composite increased, the intensity of the characteristic diffraction peak for Fe_3O_4 also increased (typically at 2θ at 35.65° and 62.91°) and the characteristic peaks of HAp decreased (typically at 2θ at 25.97° and 32.1°), corresponding to the results % of substances calculated from the peak heights characterized by XRD, Table 1.

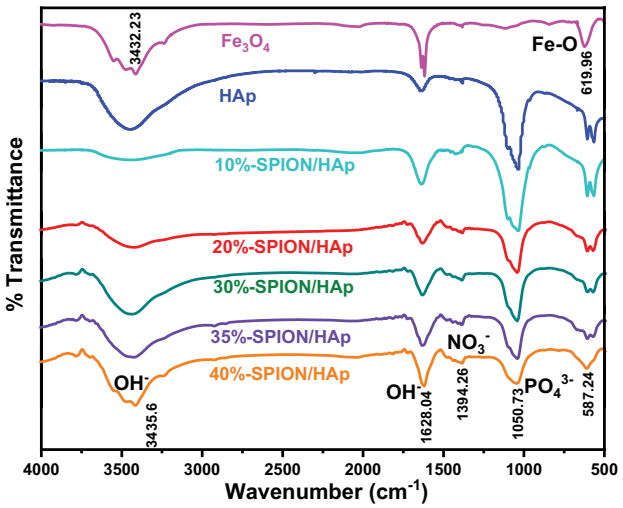

Fig. 1. Fourier-transform infrared spectra of Fe_3O_4 and Fe_3O_4/HAp.

3.1.2. EDS analysis

Additionally, the elemental analysis was performed within the EDS technique. Obtained spectra are presented in Fig. 3 and the atomic ratio is seen in Table 2. EDS results indicated that calcium, oxygen, phosphorous, and iron were in the composite's components, where the ratios of Ca/P for different composite samples range from 1.30 and 1.51. The molar ratio of Ca/P was near to standard hydroxyapatite because HAp is synthesized from apatite ore containing many impurities. On the other hand, the EDS result in Table 2 shows that Fe composition increases from 5.86% to 24.28% when the ratio of Fe_3O_4 increases from 10% to 40%.

3.1.3. Nanocomposite morphology analysis

The morphology of the nanocomposite was investigated using SEM. As can be seen in Fig. 4, the obtained structures form agglomerates (caused by the drying of the sample), where the particular structures have spherical and rod-like shapes for Fe_3O_4 and HAp, respectively. The more HAp was coated on Fe_3O_4, the more rod-like structures are obtained. Large particles can range in size from 15–20 nm. When the composite contains a higher amount of Fe_3O_4, the morphology is more homogenous with spherical shapes.

3.1.4. Brunauer–Emmett–Teller

As the proposed nanocomposite is used for the absorption of pollutants, the specific surface area was investigated.

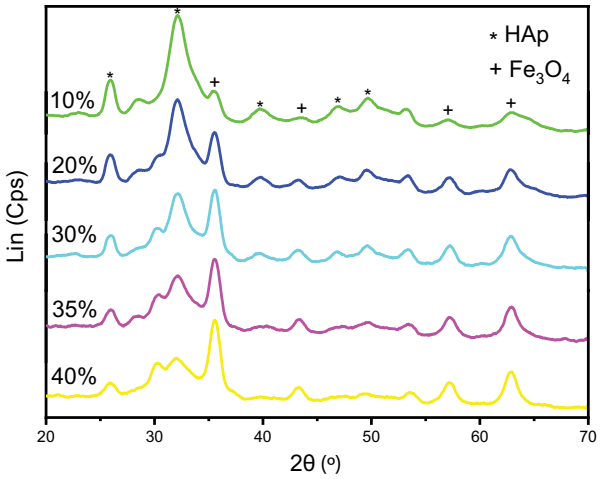

Fig. 2. X-ray diffraction patterns of Fe_3O_4/HAp.

Table 1
Ratio of SPION and HAp in composite was recorded by X-ray diffraction

	10%-SPION/HAp	20%-SPION/HAp	30%-SPION/HAp	35%-SPION/HAp	40%-SPION/HAp
% Fe_3O_4	8.1%	17.6%	23.2%	34.5%	39.3%
% HAp	91.9%	82.4%	76.8%	65.5%	60.7%

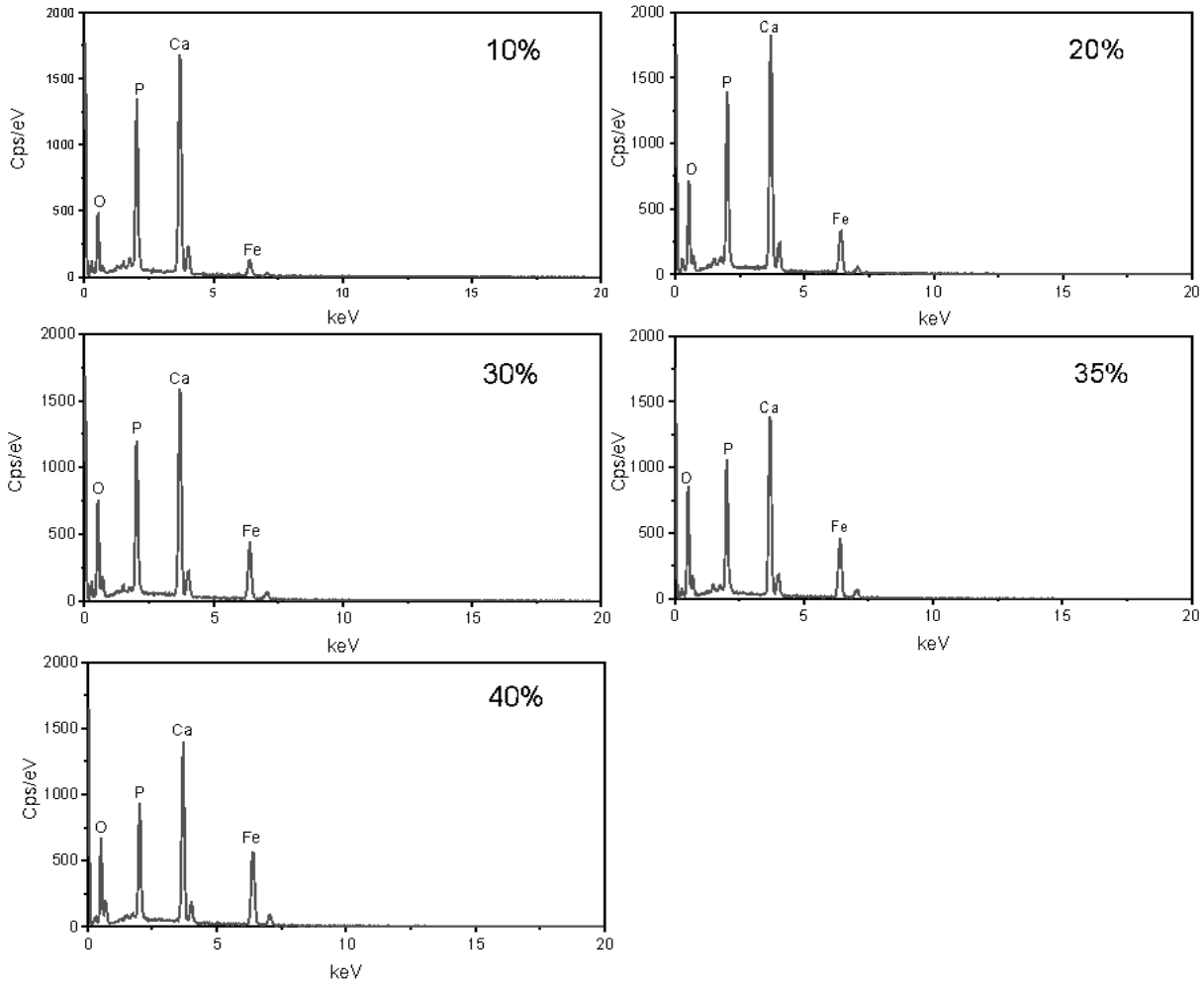

Fig. 3. Energy-dispersive X-ray spectra of Fe_3O_4/HAp with different ratios.

Table 2
Composition of elements in Fe_3O_4/HAp with different ratios

Element	10%-Fe_3O_4/HAp		20%-Fe_3O_4/HAp		30%-Fe_3O_4/HAp		35%-Fe_3O_4/HAp		40%-Fe_3O_4/HAp	
	% w	% a	% w	% a	% w	% a	% w	% a	% w	% a
O	47.60	68.15	48.00	69.50	48.40	70.43	52.84	75.08	43.39	67.15
P	16.89	12.49	14.51	10.85	13.15	9.88	10.43	7.5	11.6	9.27
Ca	29.66	16.95	25.13	14.52	22.31	12.96	17.53	9.75	20.74	12.81
Fe	5.86	2.40	12.36	5.13	16.14	6.73	19.2	7.67	24.28	10.76
Ca/P	–	1.36	–	1.51	–	1.44	–	1.30	–	1.38

The BET method was used to investigate the porosity of the material. Fig. 5a shows the nitrogen adsorption–desorption isotherms of HAp, Fe_3O_4, and Fe_3O_4/HAp, while Fig. 5b shows the BET diagram of HAp, Fe_3O_4, and Fe_3O_4/HAp. The specific surface area of the synthesized materials was calculated from the BET diagram and presented in Table 3. It can be seen that the isotherms in Fig. 5a followed the type IV adsorption isotherms defined by the IUPAC, with mesoporous properties. The hysteresis loop is classified as type B by DeBoer, and the pore can be observed in the shape of an ink-bottle [69]. The specific surface area of HAp is 216.66 $m^2 \cdot g^{-1}$, quite larger than that of Fe_3O_4 (91.37 $m^2 \cdot g^{-1}$). When the composition of Fe_3O_4 in the composite increased from 10% to 40%, the specific surface area of the material decreased. According to Table 3, the composite is mesoporous due to its size range of 6 to 12 nm. Following other studies, the HAp and its composite have potential in the treatment of pollutants [70].

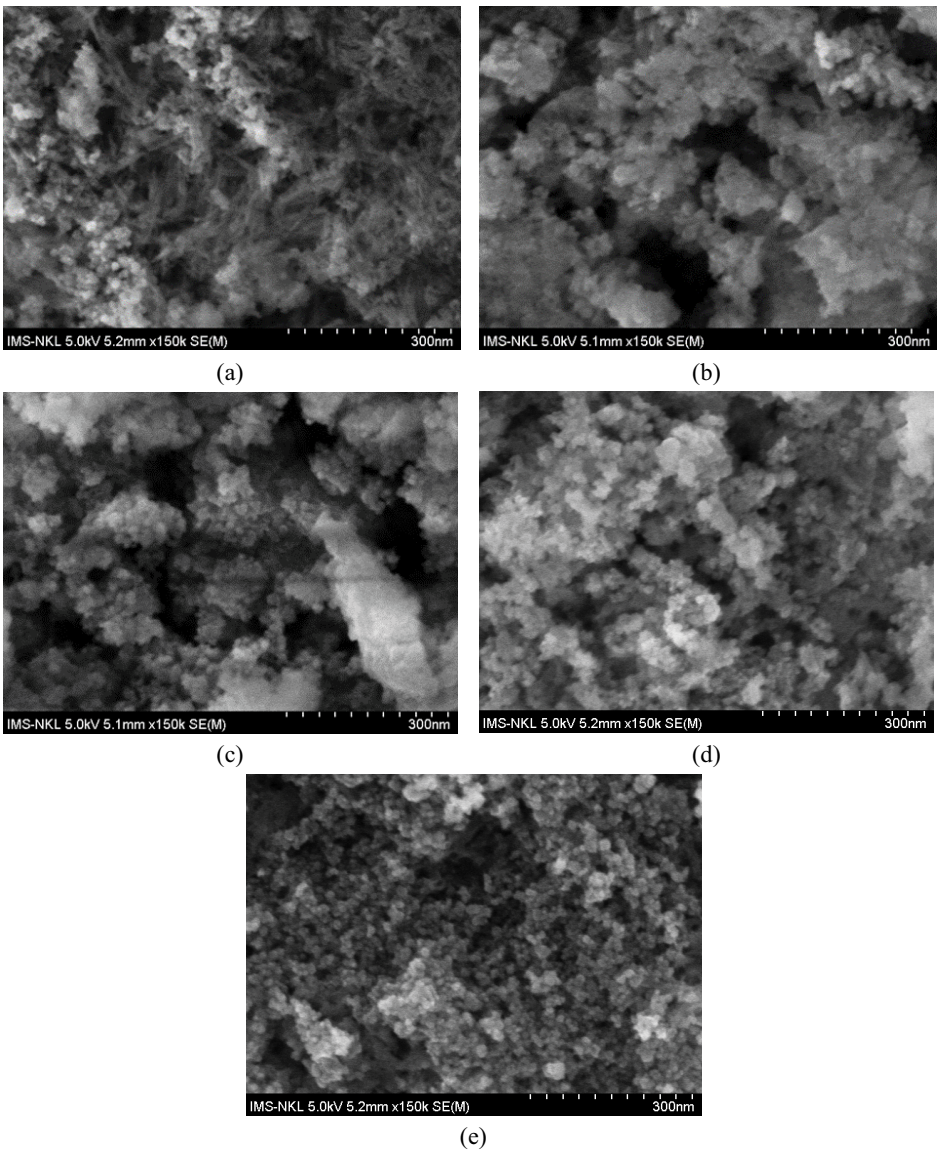

Fig. 4. Scanning electron microscopy images of 10%-Fe_3O_4/HAp (a), 20%-Fe_3O_4/HAp (b), 30%-Fe_3O_4/HAp (c), 35%-Fe_3O_4/HAp (d), and 40%-Fe_3O_4/HAp (e).

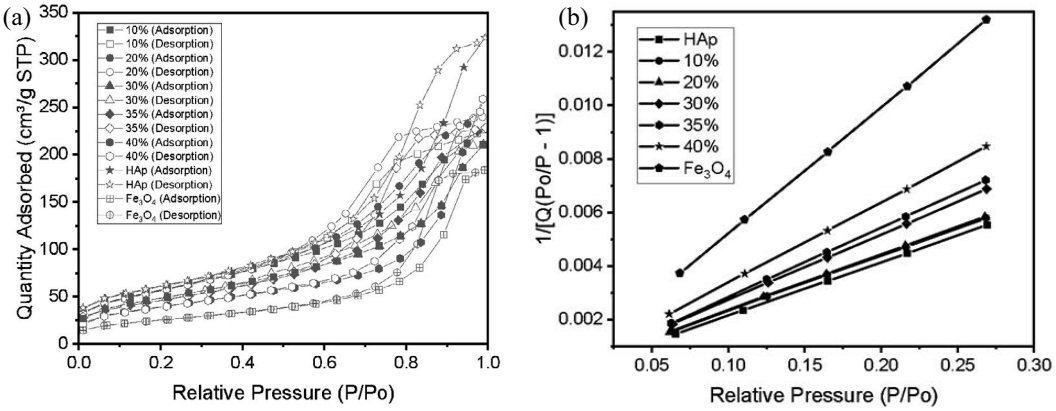

Fig. 5. N_2 adsorption–desorption isotherms (a) and Brunauer–Emmett–Teller plots (b) of HAp, Fe_3O_4, and Fe_3O_4/HAp with different ratios.

3.1.5. Magnetic properties of nanocomposite

A VSM was used to analyze the magnetic properties of the as-synthesized Fe_3O_4 and Fe_3O_4/HAp samples. As the material is dedicated to magnetic separation, the nanocomposite requires fast collection on a magnet, and a low or lack of magnetic memory is highly desired. The results are depicted in Fig. 6. For Fe_3O_4, the saturation magnetization (M_s) value at 300 K is 65.76 emu·g^{-1}, similar to the values obtained in the literature [71–73]. The M_s of Fe_3O_4/HAp increased from 4.61 to 22.91 emu·g^{-1} when the ratio of Fe_3O_4 in composite increased from 10% to 40%. The HAp surrounds the Fe_3O_4 particles, which weakens the magnetic properties for the diamagnetic character of HAp, leading to the decrease of the M_s values. The Fe_3O_4/HAp still maintains the superparamagnetic characteristics and is strong enough to be magnetically separable when a magnetic field is applied [74]. It has been reported that a M_s greater than 16.30 emu·g^{-1} is enough for magnetic separation by ordinary magnets [75]. The M_s of 35%-Fe_3O_4/HAp was 20.39 emu·g^{-1}, which is enough to separate from the solution by an external magnetic field. But when the amount of Fe_3O_4 in the composite was higher, the specific surface area decreased, which may lead to a decrease in adsorption efficiency. Therefore, the 35%-Fe_3O_4/HAp was chosen for dye adsorption.

3.2. Nanocomposite application in Congo red adsorption

3.2.1. Calibration curve

The effectiveness of the Congo red removal from aqueous media was investigated using UV-Vis spectrometry. Prior to these studies, the calibration curve in the concentration range for CR from 10 to 50 mg·L^{-1} was established (Fig. 7). The calibration equation is a linear curve: $y = 0.01226x$ with correlation coefficient $R^2 = 0.99964$ was used to determine CR concentration in the next experiments.

3.2.2. Effect of Fe_3O_4/HAp mass

Fig. 8 illustrates the effect of Fe_3O_4/HAp mass m ranging from 0.01 g to 0.15 g on the adsorption capacity and efficiency of CR during a contact time t of 4 h. It was shown that the adsorption efficiency rose rapidly from 27.31% to 75.93% when m increased from 0.01 to 0.1 g, but from 0.10 to 0.15 g the efficiency increased slightly (nearly unchanged), while the capacity decreased. Finally, m = 0.10 g was proposed as a suitable amount for further experiments to obtain not only a relatively high treatment efficiency but also a high adsorption capacity.

3.2.3. Effect of contact time

The effect of the contact time t ranging from 30 min to 6 h on the adsorption process was investigated. Fig. 9 shows an analogical trend. When t increased from 30 min to 4 h, the CR adsorption efficiency increased from 66.49% to 93.92%, and the capacity raised from 15.62 to 21.98 mg·g^{-1}. With t ranging from 4 to 6 h, the adsorption efficiency and capacity remained stable. This can be explained by the fact that when t increases, the CR fills the pores of the nanocomposite, leading to an increase in the adsorption efficiency and capacity. However, after a definite period, the adsorption equilibrium is gained, and the adsorption capacity stays nearly unchanged. Therefore, 4 h is the suitable contact time for the CR adsorption process.

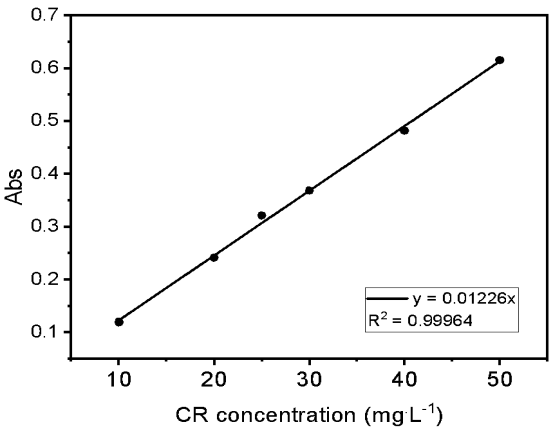

Fig. 7. Calibration curves of Congo red.

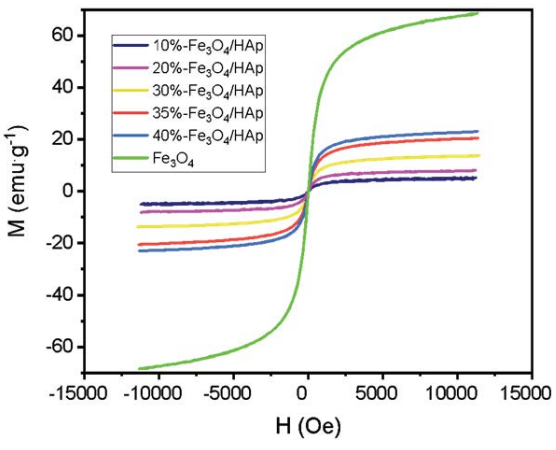

Fig. 6. Magnetization curves of Fe_3O_4 and Fe_3O_4/HAp.

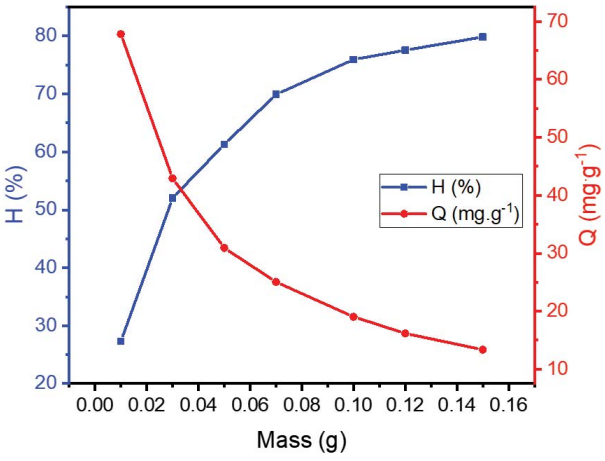

Fig. 8. Effect of Fe_3O_4/HAp mass (pH$_0$ 6.55, C_0 = 50 mg·L^{-1}, t = 4 h).

3.2.4. Adsorption kinetics

The kinetic studies of CR adsorption on the Fe_3O_4/HAp were required for finding the optimal condition towards upscaling the CR removal, where the kinetic parameters are needed for the prediction of the adsorption rate and modeling. Therefore, Lagergren's pseudo-first-order law and McKay and Ho's pseudo-second-order law model were used, where the measurements were performed in function of contact time for the optimal conditions (C_0 = 50 mg·L^{-1}, pH_0 6.55, m = 0.10 g). The equations of the two models are given in Eqs. (3) and (4), respectively [76–78]:

$$\ln\left(q_e - q_t\right) = \ln q_e - k_1 t \tag{3}$$

where q_t (mg·g^{-1}) is the adsorption capacity at time t, q_e (mg·g^{-1}) is the adsorption capacity at equilibrium, and k_1 (min^{-1}) is the pseudo-first-order adsorption rate constant.

$$\frac{t}{q_t} = \frac{1}{k_2 q_e^2} + \frac{1}{q_e} t \tag{4}$$

where k_2 (g·min^{-1}·mg^{-1}) is the pseudo-second-order rate constant for adsorption.

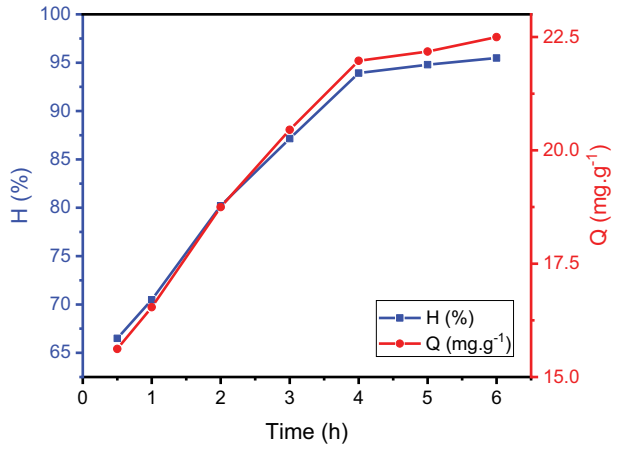

Fig. 9. Effect of contact time (C_0 = 50 mg·L^{-1}, pH_0 6.55, m = 0.10 g).

Fig. 10a shows the kinetic data using Lagergren's pseudo-first-order equation, and Fig. 10b shows the kinetic data plotted by McKay and Ho's pseudo-second-order equation. A linear trend with a high correlation coefficient (R^2 = 0.99721) between t/q_t and t was obtained, suggesting that the CR adsorption on the composite was fitted with the pseudo-second-order model than the pseudo-first-order one. The calculated parameters of this model are presented in Table 4.

3.2.5. pH value at the point of zero charge (pH_{pzc})

The pH_{pzc} is the pH value at which the static charge on the surface of the adsorbent is equal to zero. The pH_{pzc} was measured according to the literature reported by Lei et al. [79]. The pH_{pzc} results of the nanocomposite are shown in Fig. 11. The adsorbent has the point of zero charge at pH_{pzc} 7.05. Depending on the pH of the adsorption medium, the

Table 3
Surface area and pore analysis of materials

	Surface area ($m^2 \cdot g^{-1}$)	Pore volume ($cm^3 \cdot g^{-1}$)	Pore size (nm)
Bare HAp	216.66	0.49	9.23
10%-Fe_3O_4/HAp	208.73	0.35	6.61
20%-Fe_3O_4/HAp	206.58	0.38	6.69
30%-Fe_3O_4/HAp	175.61	0.32	7.59
35%-Fe_3O_4/HAp	166.11	0.35	8.13
40%-Fe_3O_4/HAp	143.70	0.40	11.44
Bare Fe_3O_4	91.37	0.28	12.05

Table 4
Parameters of the Congo red removal process calculated using McKay and Ho's pseudo-second-order law model

Linear equation	$q_{e,exp}$ (mg·g^{-1})	$q_{e,cal}$ (mg·g^{-1})	k_2 (g·mg^{-1}·min^{-1})	R^2
y = 0.04256x + 0.01731	24.50	23.50	0.104642	0.99721

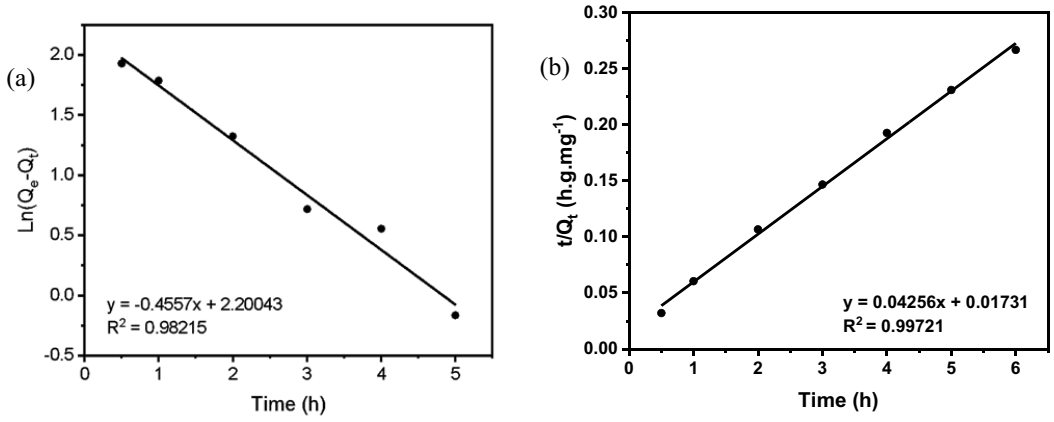

Fig. 10. Adsorption data modeled using kinetic models: (a) Lagergren's pseudo-first-order law and (b) McKay and Ho's pseudo-second-order law.

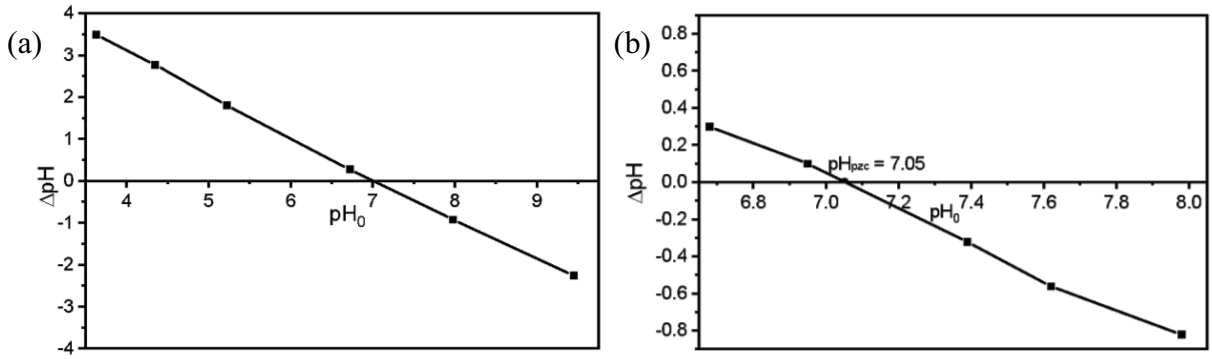

Fig. 11. pH_{pzc} of 35%-Fe_3O_4/HAp in both a wide pH range (a) and a narrow pH range (b).

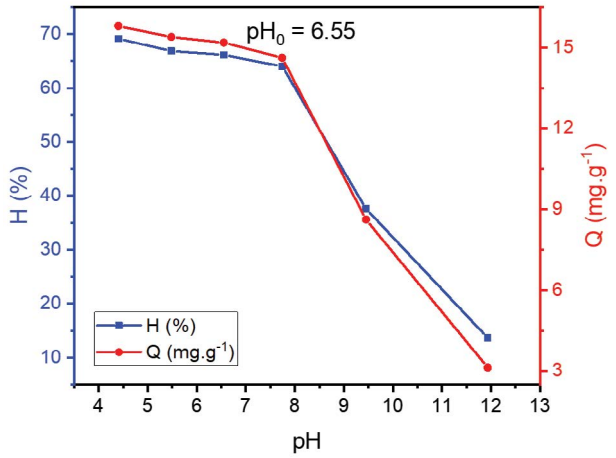

Fig. 12. Variation of adsorption efficiency and capacity follow pH with the mass of composite = 0.10 g, C_0 = 50 mg·L^{-1}, contact time = 4 h.

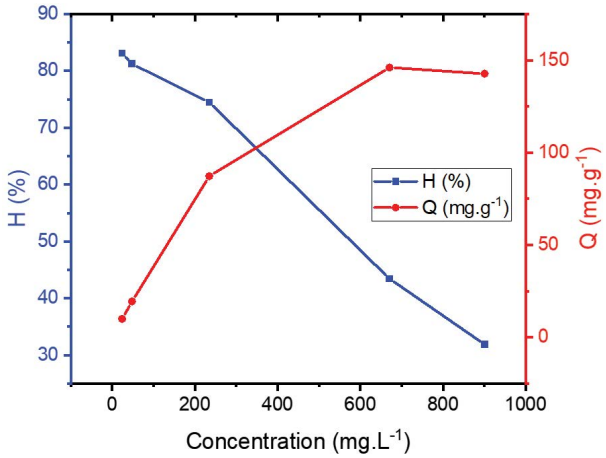

Fig. 13. Effect of initial Congo red concentration (m = 0.10 g, pH_0 6.55, t = 4 h).

surface of the material has a positive or negative charge. If the adsorption is carried out at pH < pH_{pzc} 7.05, the material surface has a positive charge, whereas, with a pH > 7.05, the surface of the material has a negative charge [80]. The determined pH_{pzc} values can be served as a basis for explaining the dependency of the adsorption capacity of the material on the pH of the environment.

3.2.6. Effect of pH

It is reported that the pH of the solution is an important factor that alters the adsorption efficiency [81]. The pH of the initial solution of CR in the adsorption process of the composite varied from 4 to 12. Fig. 12 shows the effect of initial pH on the CR removal efficiency. It is observed that the removal efficiency decreases as the pH increases. To further analyze the effect of pH on adsorption efficiency, the point of zero charge value (pH_{pzc}) was determined. As shown in Fig. 11, pH_{pzc} of Fe_3O_4/HAp is measured to be 7.05. The adsorbent is positively charged when the solution pH < 7.05, thereby attracting the anionic dye CR. Moreover, the concentration of OH^- in the solution increases in an alkaline environment, and OH^- is competition for the free adsorption site with anionic dye, resulting in a decrease in CR removal efficiency. Therefore, the electrostatic attraction could be the main adsorption mechanism. A similar effect of the initial solution pH on the adsorption of CR onto m-cell/Fe_3O_4/ACCs [82] and Fe_3O_4/CLAP [17] was reported in previous studies. A relatively low pH is more favourable for adsorption. At pH_0 6.55 (unadjusted) the efficiency was 66.14%, not significantly different from that at pH 4.40 (69.15%). Thus, in order not to have to adjust, the initial pH was fixed at pH_0 6.55 for other experiments.

3.2.7. Effect of initial CR concentration

The effect of the initial CR concentration C_0 ranging from 25 to 900 mg·L^{-1} on the adsorption efficiency and capacity of Fe_3O_4/HAp was investigated. Fig. 13 shows that when C_0 increased, the adsorption efficiency decreased, and the capacity rose. When C_0 varied to a definite value, the adsorption capacity reached the saturated state. With a certain amount of Fe_3O_4/HAp, there are a specified number of adsorption sites. In the case of all the adsorption sites being full by the CR ion, when the concentration of Congo red increases, the adsorption capacity nearly has no change.

3.2.8. Maximum adsorption capacity

The adsorption experiments were conducted under the following conditions: 0.10 g of composite in 50 mL of CR solution with varied concentrations, stirred in 4 h with a speed of 250 rpm. To better understand the adsorption process, two isotherm models are used to evaluate the experimental data. The expressions are shown as equations.

Langmuir isotherm:

$$\frac{C_e}{q_e} = \frac{1}{q_m K_L} + \frac{C_e}{q_m} \tag{5}$$

Freundlich isotherm:

$$R_L = \frac{1}{1 + K_L C_0} \tag{6}$$

$$\log q_e = \log K_F + \frac{1}{n} \log C_e \tag{7}$$

where q_e and q_m (mg·g^{-1}) represent the equilibrium adsorption capacity and the maximum adsorption capacity calculated from the Langmuir isotherm. K_L (L·mg^{-1}) and K_F ((mg·g^{-1})(L·mg^{-1})$^{1/n}$) represent the constants of these two models. The R_L is related to whether an isotherm is unfavorable ($R_L > 1$), linear ($R_L = 1$), favorable ($0 < R_L < 1$), and irreversible ($R_L = 0$). The $1/n$ is related to the intensity of adsorption. The adsorption is favorable when $1/n < 1$.

Langmuir isotherm theory assumes that the process is monolayer adsorption on a homogeneous adsorbent surface with a limited adsorption site amount whereas Freundlich's model indicates that the adsorption process is not restricted to a monolayer adsorption process [83,84].

Fig. 14 shows the data fitting curves and the isotherm parameters are listed in Table 5. Langmuir's model described the adsorption behaviour well with a relatively high R^2 value. The maximum adsorption capacity $q_{e,exp}$ (146.03 mg·g^{-1}) obtained by the experiments is close to $q_{e,cal}$ (158.98 mg·g^{-1}) calculated from the Langmuir isotherm, indicating that the Langmuir model is applicable for the adsorption of CR onto Fe_3O_4/HAp. Therefore, the adsorption of CR onto Fe_3O_4/HAp can be expected as a favourably homogeneous monolayer adsorption process. A similar result has been reported in the adsorption of CR onto hierarchical NiO-SiO_2 [79]. Due to the R^2 of the Freundlich isotherm model, the value is only 0.93955 (30°C), so it can be concluded that such an isotherm model is not suitable for the adsorption process.

The maximum adsorption capacity of Fe_3O_4/HAp on CR is 158.98 mg·g^{-1}, which is higher or comparable with values of adsorption capacity described for magnetic materials selected from the literature, Table 6.

3.2.9. Effect of temperature

When the temperature of the adsorption process increased, the adsorption efficiency and capacity decreased (Table 7). The thermodynamic parameters, including the standard Gibb's free energy change ($\Delta G°$), the enthalpy change ($\Delta H°$), and the entropy change ($\Delta S°$) of the adsorption of CR onto Fe_3O_4/HAp are specified using the following equations:

$$\Delta G° = -RT \ln K_d \tag{8}$$

$$\ln K_d = -\frac{\Delta H°}{R} \times \frac{1}{T} + \frac{\Delta S°}{R} \tag{9}$$

Table 5
Isotherm parameters of adsorption of Congo red onto Fe_3O_4/HAp

Langmuir			Freundlich		
q_m (mg·g^{-1})	K_L (L·mg^{-1})	R^2	K_F ((mg·g^{-1})(L·mg^{-1}))$^{1/n}$	$1/n$	R^2
158.98	0.018	0.9972	60.31	1.860	0.9396

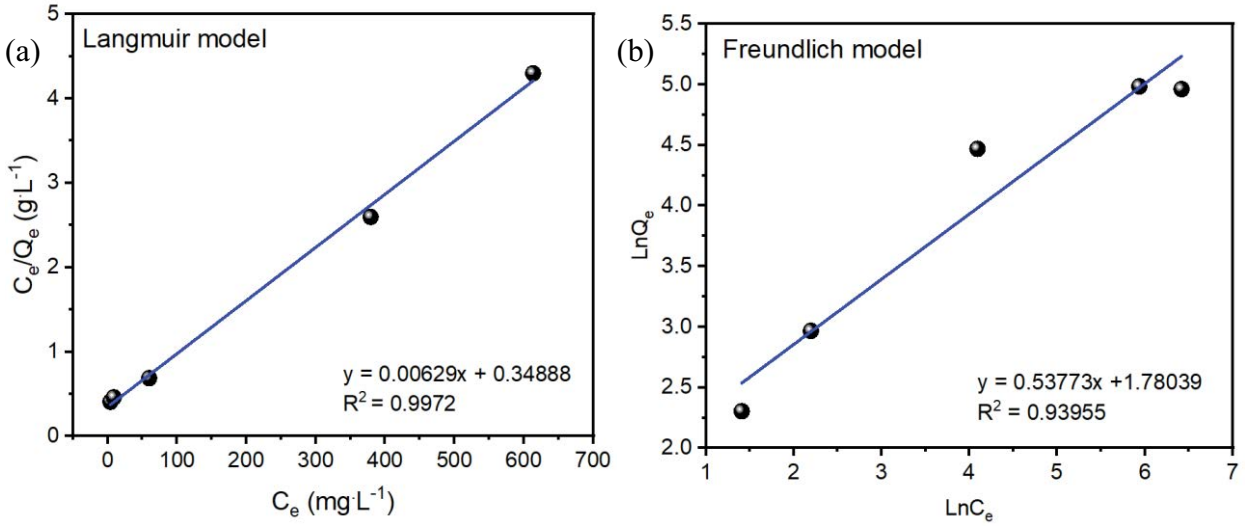

Fig. 14. Adsorption isotherm curves of Congo red follow the Langmuir model (a) and Freundlich (b).

Table 6
Comparison of adsorption capacities of various adsorbents for Congo red removal

Adsorbents	Adsorption conditions	q_{max} (mg·g^{-1})	References
Bentonite	pH 5.8, 25°C	68.96	[30]
Chitosan/montmorillonite	pH 7, 30°C	54.52	[31]
Coir pith	pH 7.70, 35°C	6.72	[32]
KJA/Ti	25°C	52.00	[33]
KJA/N/café	25°C	159.00	[33]
SA/N/café	25°C	161.00	[33]
KJA/S/café	25°C	189.00	[33]
Activated red mud	pH 7	7.08	[34]
Neem leaf powder	pH 6.7, 25°C	41.2	[36]
Chitosan hydrobeads	pH ~ 6.0, 30°C ± 1°C	65.77	[38]
Pine bark	pH 2–9, 25°C–60°C	0.3–1.6	[85]
Industrial waste	pH 7, 25°C	22.12	[10]
Ash-fly@Fe_3O_4	pH 6.5–7	154	[86]
Breadfruit leaf biochar	pH 6.37	17.81	[87]
Magnetic HKUST-1	pH 7, 25°C	49.5	[88]
Kaolin-aminated-chitosan	pH 7, 25°C	104.16	[89]
Magnetic nanocellulose based ionic liquid	pH 6.8, 25°C	102.4	[89]
Fe_3O_4/HAp	pH 6.55, 28°C	158.98	This work

Table 7
Parameters H (%), Q_e (mg·g^{-1}), and K_d when temperature varies in the Congo red adsorption process (t = 4 h, m = 0.10 g, pH_o 6.55)

T (K)	C_0 (mg·L^{-1})	C_e (mg·L^{-1})	H (%)	Q_e (mg·g^{-1})	$K_d = Q_e/C_e$	lnK_d	1/T
301		23.74	50.26	11.98	0.50	–0.68	0.003322
308		23.33	51.11	12.16	0.52	–0.65	0.003247
318	47.72	30.42	36.24	8.60	0.28	–1.26	0.003145
328		36.79	22.91	5.48	0.15	–1.90	0.003049
338		39.15	17.95	4.30	0.11	–2.21	0.002959

where R is the universal gas constant (8.314 J·mol^{-1}·K^{-1}), T is the temperature (K), and K_d is the equilibrium constant. The intercept and slope of the plot of lnK_d vs. 1/T (Fig. 15) give the values of $\Delta G°$, $\Delta H°$, and $\Delta S°$ (Table 8). A positive value of $\Delta G°$ and a negative value of $\Delta H°$ showed that the adsorption process was non-spontaneous and exothermic. The $\Delta S°$ with negative values proved the decrease in randomness at the adsorbate–adsorbent interface.

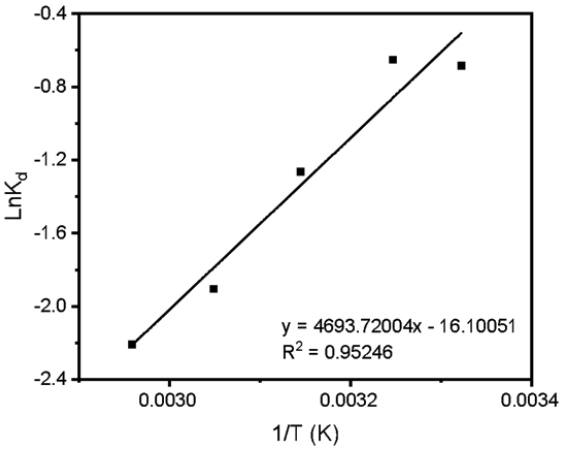

Fig. 15. Relationship between lnK_d and 1/T.

3.3. Mechanism studies

The adsorption mechanism could be described as the interaction between the CR molecules and the surface of the adsorbent. Based on the pH studies and the compositional studies of the adsorbent using FT-IR, it can be concluded that the CR adsorption on the surface of Fe_3O_4/HAp undergoes the Langmuir model assuming that CR is adsorbed on the binding or active sites of the adsorbent's surface, where the adsorption sites are energetically comparable [90]. Each molecule of CR reaches each active site on time forming a monolayer. As the CR is an ionic dye dissociating in low pH to a polar group (R-SO_3–), it interacts with the positively charged surface of the material in acidic pH ($pH < pH_{pzc}$) [90,91]. At the same time, the opposing charges on the adsorbent's surface and the CR molecule enhance electrostatic interactions [92]. Besides Coulomb interactions, the adsorption process also undergoes hydrogen

Table 8
Parameters $\Delta H°$, $\Delta S°$, $\Delta G°$

T (K)	$\Delta H°$ (kJ·mol^{-1})	$\Delta S°$ (kJ·mol^{-1}·K^{-1})	$\Delta G° = \Delta H° - T\Delta S°$ (kJ·mol^{-1})	$\Delta G° = -RT\ln K_d$
301			1.27	1.71
308			2.21	1.67
318	–39.02	–0.134	3.54	3.34
328			4.88	5.19
338			6.22	6.21

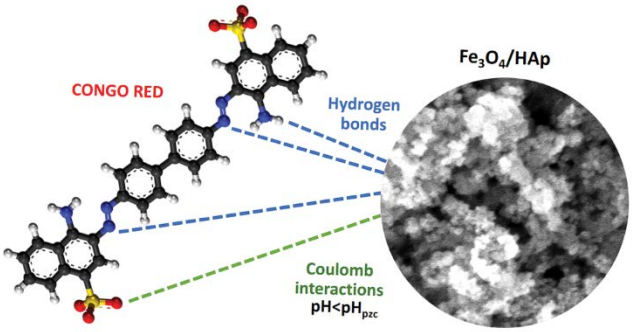

Fig. 16. Proposed mechanism of Congo red adsorption on Fe_3O_4/HAp.

bonding. Fig. 16 presents a schematic image describing the mechanism of CR adsorption on the Fe_3O_4/HAp surface.

3.4. Reusability studies

From the practical and economical point of view, another factor closely related to the potential of upscaled application of adsorbent is the number of cycles of operation. So far, the reusability was investigated using the optimal conditions, namely 4 h contact time, 0.10 g of 35%-Fe_3O_4/HAp adsorbent, 50 mL of 50 mg·L^{-1} CR, and pH_o 6.55. Then, the adsorbent was separated magnetically from the CR solution and placed in 50 mL of 0.1 M NaOH solution with stirring at about 150 rpm for 4 h for desorption of the anionic dye. Initially, the ethanol was tested as eluent; however, the effectiveness was not satisfactory. Thus, for the more economical reuse of adsorbent, NaOH was chosen. Messaoudi et al. [93] also refer to NaOH as the more effective eluent for CR desorption than alcohols. After 4 h treatment, the adsorbent was separated magnetically from the NaOH solution containing desorbed CR, washed with distilled water, and dried in the oven. Then, the Fe_3O_4/HAp was placed directly into the fresh CR solution, where the dye solution was exposed to the adsorbent in the same way. The adsorption/desorption was performed 5 times for the same material. As can be seen in Fig. 17 the effectiveness of CR removal after the first cycle is about ~63%, while the desorption reaches nearly 83%. Then, within the second cycle the adsorption yield H% increased and remains about 65% effective for subsequent 3–5 cycles likewise the iron-based or Ca-based materials presented in the literature [94–96], and in the desorption process, it is seen that the H% tend to decrease. Decreasing effectiveness may be

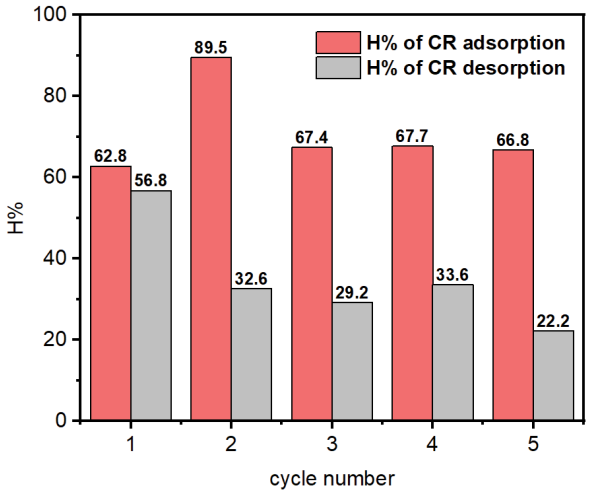

Fig. 17. Adsorption and desorption yield H% in the function of cycles operation.

related to the blocking of the adsorbent's surface with CR or compositional changes of the surface after the NaOH treatment.

4. Conclusion

The SPION/HAp nanocomposite synthesized by the co-precipitation method using the apatite ore as a HAp precursor is a promising material for water purification. In addition, the synthesis of HAp from the apatite ore found in Lao Cai – Vietnam is a useful solution when taking advantage of available resources. The morphology of the composite depends on the HAp content, where its increase leads to the formation of rod-like structures. The FT-IR results confirm the presence of functional groups of both Fe_3O_4 and HAp such as Fe–O, O–H, and PO_4^{3-}. The specific surface area of 35%-Fe_3O_4/HAp is high (166.11 m^2·g^{-1}) contributing to the treatment of pollutants. The superparamagnetic properties of the Fe_3O_4/HAp nanoparticles are still ensured which is suitable for magnetic separation from the solution. The application of nanocomposite towards the Congo red removal from aqueous media is cost-effective, easy to operate, and makes it possible to remove the adsorbent magnetically. A suitable condition for the adsorption of 50 mL of 50 mg·L^{-1} CR solution was determined with a contact time of 4 h, 0.10 g of material, and pH_0 6.55. The Fe_3O_4/HAp composite has a maximum adsorption capacity value of 158.98 mg·g^{-1} and follows the Langmuir isotherm

adsorption model, where the interactions between the adsorbent and adsorbate are mainly based on the hydrogen bonds and Coulomb interactions. The pseudo-second-order kinetic model has more potential in describing the kinetic behaviour of the process than the pseudo-first-order kinetic. The thermodynamic parameters such as enthalpy ($\Delta H°$), entropy ($\Delta S°$), and Gibbs free energy ($\Delta G°$) highlighted that the adsorption of CR using the SPION/HAp nanoparticles is exothermal and non-spontaneous. The obtained material was used within the 5 cycles of operation offering its reusability.

Funding

This research was funded by the Vietnam Academy of Science and Technology (VAST) with grant no. NCVCC13.07/22-23 and Hanoi University of Mining and Geology with grant no. T22-20.

Conflict of interest

The authors declare no conflict of interest.

References

[1] X. Liu, L. Yan, W. Yin, L. Zhou, G. Tian, J. Shi, Z. Yang, D. Xiao, Z. Gu, Y. Zhao, A magnetic graphene hybrid functionalized with beta-cyclodextrins for fast and efficient removal of organic dyes, J. Mater. Chem. A, 2 (2014) 12296, doi: 10.1039/C4TA00753K.
[2] V.S. Munagapati, D.-S. Kim, Equilibrium isotherms, kinetics, and thermodynamics studies for Congo red adsorption using calcium alginate beads impregnated with nano-goethite, Ecotoxicol. Environ. Saf., 141 (2017) 226–234.
[3] D. Gautam, S. Kumari, B. Ram, G.S. Chauhan, K. Chauhan, A new hemicellulose-based adsorbent for malachite green, J. Environ. Chem. Eng., 6 (2018) 3889–3897.
[4] N.B. Swan, M.A.A. Zaini, Adsorption of Malachite green and Congo red dyes from water: recent progress and future outlook, Ecol. Chem. Eng. S, 26 (2019) 119–132.
[5] K. Naseem, Z.H. Farooqi, R. Begum, A. Irfan, Removal of Congo red dye from aqueous medium by its catalytic reduction using sodium borohydride in the presence of various inorganic nano-catalysts: a review, J. Cleaner Prod., 187 (2018) 296–307.
[6] R. Rehman, S. Abbas, S. Murtaza, T. Mahmud, W. Zaman, M. Salman, U. Shafique, Comparative removal of Congo red dye from water by adsorption on *Grewia asiatica* leaves, *Raphanus sativus* peels and activated charcoal, J. Chem. Soc. Pak., 34 (2012) 112–119.
[7] R. Septiawan, E. Amiruddin, A. Awaluddin, H. Hadianto, N. Davini, Synthesis of magnetic iron oxide nanoparticle from logas natural sand and its application for the catalytic degradation of Methylene blue, J. Phys.: Conf. Ser., 1655 (2020) 012014, doi: 10.1088/1742-6596/1655/1/012014.
[8] N.P. Raval, P.U. Shah, N.K. Shah, Adsorptive amputation of hazardous azo dye Congo red from wastewater: a critical review, Environ. Sci. Pollut. Res., 23 (2016) 14810–14853.
[9] R. Kishor, D. Purchase, G.D. Saratale, L.F.R. Ferreira, M. Bilal, H.M.N. Iqbal, R.N. Bharagava, Environment friendly degradation and detoxification of Congo red dye and textile industry wastewater by a newly isolated *Bacillus cohnni* (RKS9), Environ. Technol. Innovation, 22 (2021) 101425, doi: 10.1016/j.eti.2021.101425.
[10] M. Harja, G. Buema, D. Bucur, Recent advances in removal of Congo red dye by adsorption using an industrial waste, Sci. Rep., 12 (2022) 6087, doi: 10.1038/s41598-022-10093-3.
[11] P.O. Oladoye, M.O. Bamigboye, O.D. Ogunbiyi, M.T. Akano, Toxicity and decontamination strategies of Congo red dye, Groundwater Sustainable Dev., 19 (2022) 100844, doi: 10.1016/j.gsd.2022.100844.
[12] S.I. Siddiqui, E.S. Allehyani, S.A. Al-Harbi, Z. Hasan, M.A. Abomuti, H.K. Rajor, S. Oh, Investigation of Congo red toxicity towards different living organisms: a review, Processes, 11 (2023) 807, doi: 10.3390/pr11030807.
[13] M.S. Hussain, R. Rehman, M. Imran, A. Dar, M. Akram, E.A. Al-Abbad, Eco-friendly detoxification of Congo red dye from water by citric acid activated bioadsorbents consisting of watermelon and water chestnuts peels collected from indigenous resources, Adsorpt. Sci. Technol., 2022 (2022) e9056288, doi: 10.1155/2022/9056288.
[14] S. Basharat, R. Rehman, S. Basharat, Adsorptive behavior of tartaric acid treated *Holarrhena antidysenterica* and *Citrullus colocynthis* biowastes for decolourization of Congo red dye from aqueous solutions, J. Chem., 2022 (2022) e5724347, doi: 10.1155/2022/5724347.
[15] A. Afkhami, R. Moosavi, Adsorptive removal of Congo red, a carcinogenic textile dye, from aqueous solutions by maghemite nanoparticles, J. Hazard. Mater., 174 (2010) 398–403.
[16] A. Ausavasukhi, C. Kampoosaen, O. Kengnok, Adsorption characteristics of Congo red on carbonized leonardite, J. Cleaner Prod., 134 (2016) 506–514.
[17] J. Wang, Y. Liu, H. Xie, P. Li, X. Chen, W. Hu, Y. Wang, Y. Zhang, Facile synthesis of a magnetic chlorapatite composite with a high efficiency and recyclable adsorption for Congo red, Mater. Res. Express, 6 (2019) 116118, doi: 10.1088/2053-1591/ab4b9c.
[18] R. Rehman, F. Kanwal, L. Mitu, Microwave treated *Gardenia jasminoides* leaves for adsorptive removal of Direct red-28 dye in environmental benign way, Rev. de Chim., 69 (2019) 3445–3450.
[19] C. Wang, Y. Zhang, L. Yu, Z. Zhang, H. Sun, Oxidative degradation of azo dyes using tourmaline, J. Hazard. Mater., 260 (2013) 851–859.
[20] M.F. Elahmadi, N. Bensalah, A. Gadri, Treatment of aqueous wastes contaminated with Congo red dye by electrochemical oxidation and ozonation processes, J. Hazard. Mater., 168 (2009) 1163–1169.
[21] P.V. Nidheesh, M. Zhou, M.A. Oturan, An overview on the removal of synthetic dyes from water by electrochemical advanced oxidation processes, Chemosphere, 197 (2018) 210–227.
[22] A. Lahkimi, M.A. Oturan, N. Oturan, M. Chaouch, Removal of textile dyes from water by the electro-Fenton process, Environ. Chem. Lett., 5 (2007) 35–39.
[23] B. Lodha, S. Chaudhari, Optimization of Fenton-biological treatment scheme for the treatment of aqueous dye solutions, J. Hazard. Mater., 148 (2007) 459–466.
[24] A. Ahmedi, M. Abouseoud, A. Abdeltif, C. Annabelle, Effect of diffusion on discoloration of Congo red by alginate entrapped turnip (*Brassica rapa*) peroxidase, Enzyme Res., 2015 (2015) 1–9.
[25] S. Sachdeva, A. Kumar, Preparation of nanoporous composite carbon membrane for separation of Rhodamine B dye, J. Membr. Sci., 329 (2009) 2–10.
[26] L.G. Devi, B.N. Murthy, S.G. Kumar, Photocatalytic activity of TiO_2 doped with Zn^{2+} and V^{5+} transition metal ions: influence of crystallite size and dopant electronic configuration on photocatalytic activity, Mater. Sci. Eng., B, 166 (2010) 1–6.
[27] M. Punzi, F. Nilsson, A. Anbalagan, B.-M. Svensson, K. Jönsson, B. Mattiasson, M. Jonstrup, Combined anaerobic–ozonation process for treatment of textile wastewater: removal of acute toxicity and mutagenicity, J. Hazard. Mater., 292 (2015) 52–60.
[28] C.H. Neoh, C.Y. Lam, C.K. Lim, A. Yahya, H.H. Bay, Z. Ibrahim, Z.Z. Noor, Biodecolorization of recalcitrant dye as the sole source of nutrition using *Curvularia clavata* NŽ2 and decolorization ability of its crude enzymes, Environ. Sci. Pollut. Res., 22 (2015) 11669–11678.
[29] S. Hokkanen, B. Doshi, V. Srivastava, L. Puro, R. Koivula, Arsenic(III) removal from water by hydroxyapatite-bentonite clay-nanocrystalline cellulose, Environ. Prog. Sustainable Energy, 38 (2019) 13147, doi: 10.1002/ep.13147.

[30] Z. Zhang, Y. Li, Q. Du, Q. Li, Adsorption of Congo red from aqueous solutions by porous soybean curd xerogels, Pol. J. Chem. Technol., 20 (2018) 95–102.
[31] L. Wang, A. Wang, Adsorption characteristics of Congo red onto the chitosan/montmorillonite nanocomposite, J. Hazard. Mater., 147 (2007) 979–985.
[32] C. Namasivayam, D. Kavitha, Removal of Congo red from water by adsorption onto activated carbon prepared from coir pith, an agricultural solid waste, Dyes Pigm., 54 (2002) 47–58.
[33] E. Lorencgrabowska, G. Gryglewicz, Adsorption characteristics of Congo red on coal-based mesoporous activated carbon, Dyes Pigm., 74 (2007) 34–40.
[34] A. Tor, Y. Cengeloglu, Removal of Congo red from aqueous solution by adsorption onto acid activated red mud, J. Hazard. Mater., 138 (2006) 409–415.
[35] K.-S. Chou, J.-C. Tsai, C.-T. Lo, The adsorption of Congo red and vacuum pump oil by rice hull ash, Bioresour. Technol., 78 (2001) 217–219.
[36] K.G. Bhattacharyya, A. Sharma, *Azadirachta indica* leaf powder as an effective biosorbent for dyes: a case study with aqueous Congo red solutions, J. Environ. Manage., 71 (2004) 217–229.
[37] R. Han, D. Ding, Y. Xu, W. Zou, Y. Wang, Y. Li, L. Zou, Use of rice husk for the adsorption of Congo red from aqueous solution in column mode, Bioresour. Technol., 99 (2008) 2938–2946.
[38] S. Chatterjee, S. Chatterjee, B.P. Chatterjee, A.K. Guha, Adsorptive removal of Congo red, a carcinogenic textile dye by chitosan hydrobeads: Binding mechanism, equilibrium and kinetics, Colloids Surf., A, 299 (2007) 146–152.
[39] Y. Guan, W. Cao, X. Wang, A. Marchetti, Y. Tu, Hydroxyapatite nano-rods for the fast removal of Congo red dye from aqueous solution, Mater. Res. Express, 5 (2018) 065053, doi: 10.1088/2053-1591/aaccb8.
[40] J. Jiang, Y. Long, X. Hu, J. Hu, M. Zhu, S. Zhou, A facile microwave-assisted synthesis of mesoporous hydroxyapatite as an efficient adsorbent for Pb^{2+} adsorption, J. Solid State Chem., 289 (2020) 121491, doi: 10.1016/j.jssc.2020.121491.
[41] K. Bouiahya, I. Es-saidi, C.E. Bekkali, A. Laghzizil, D. Robert, J.M. Nunzi, A. Saoiabi, Synthesis and properties of alumina-hydroxyapatite composites from natural phosphate for phenol removal from water, Colloid Interface Sci. Commun., 31 (2019) 100188, doi: 10.1016/j.colcom.2019.100188.
[42] W. Wei, R. Sun, Z. Jin, J. Cui, Z. Wei, Hydroxyapatite–gelatin nanocomposite as a novel adsorbent for nitrobenzene removal from aqueous solution, Appl. Surf. Sci., 292 (2014) 1020–1029.
[43] M. Harja, G. Ciobanu, Studies on adsorption of oxytetracycline from aqueous solutions onto hydroxyapatite, Sci. Total Environ., 628–629 (2018) 36–43.
[44] G.N. Kousalya, M.R. Gandhi, C.S. Sundaram, S. Meenakshi, Synthesis of nano-hydroxyapatite chitin/chitosan hybrid biocomposites for the removal of Fe(III), Carbohydr. Polym., 82 (2010) 594–599.
[45] Y. Zhou, W. Li, X. Jiang, Y. Sun, H. Yang, Q. Liu, Y. Cao, Y. Zhang, H. Cheng, Synthesis of strontium (Sr) doped hydroxyapatite (HAp) nanorods for enhanced adsorption of Cr(VI) ions from wastewater, Ceram. Int., 47 (2021) 16730–16736.
[46] P.N. Nam, D.T.M. Thanh, N.T. Phuong, N.T.T. Trang, C.T. Hong, V.T.K. Anh, T.D. Lam, N.T. Thom, Adsorption of Ag^{+} ions using hydroxyapatite powder and recovery silver by electrodeposition, Vietnam J. Chem., 59 (2021) 179–186.
[47] P.T. Nguyen, X.T. Nguyen, T.V. Nguyen, T.T. Nguyen, T.Q. Vu, H.T. Nguyen, N.T. Pham, T.M.T. Dinh, Treatment of Cd^{2+} and Cu^{2+} ions using modified apatite ore, J. Chem., 2020 (2020) 1–12, doi: 10.1155/2020/6527197.
[48] S. Pai, S.M. Kini, R. Selvaraj, A. Pugazhendhi, A review on the synthesis of hydroxyapatite, its composites and adsorptive removal of pollutants from wastewater, J. Water Process Eng., 38 (2020) 101574, doi: 10.1016/j.jwpe.2020.101574.
[49] I. Nikčević, V. Jokanović, M. Mitrić, Z. Nedić, D. Makovec, D. Uskoković, Mechanochemical synthesis of nanostructured fluorapatite/fluorhydroxyapatite and carbonated fluorapatite/fluorhydroxyapatite, J. Solid State Chem. 177 (2004) 2565–2574.
[50] D.L. Thi, T.L.T. Phuong, H.V. Thi, T.D.T. Mai, Research on adsorption of Zn^{2+} by hydroxyapatite/chitosan nanocomposite, Vietnam J. Catal. Adsorpt., 9 (2020) 62–69.
[51] N.T. Thom, D.T.M. Thanh, P.T. Nam, N.T. Phuong, C. Buess-Herman, Adsorption behavior of Cd^{2+} ions using hydroxyapatite (HAp) powder, Green Process. Synth., 7 (2018) 409–416.
[52] Wahajuddin, S. Arora, Superparamagnetic iron oxide nanoparticles: magnetic nanoplatforms as drug carriers, Int. J. Nanomed., (2012) 3445, doi: 10.2147/IJN.S30320.
[53] S.J. Olusegun, T.G.F. Souza, G. de O. Souza, M. Osial, N.D.S. Mohallem, V.S.T. Ciminelli, P. Krysinski, Iron-based materials for the adsorption and photocatalytic degradation of pharmaceutical drugs: a comprehensive review of the mechanism pathway, J. Water Process Eng., 51 (2023) 103457, doi: 10.1016/j.jwpe.2022.103457.
[54] M. Żuk, W. Gawęda, A. Majkowska-Pilip, M. Osial, M. Wolski, A. Bilewicz, P. Krysiński, Hybrid radiobioconjugated superparamagnetic iron oxide-based nanoparticles for multimodal cancer therapy, Pharmaceutics, 13 (2021) 1843, doi: 10.3390/pharmaceutics13111843.
[55] S.J. Olusegun, M. Osial, A. Majkowska-Pilip, K. Żelechowska-Matysiak, D. Nieciecka, M. Krajewski, M. Pękała, P. Krysinski, Synthesis and characterization of Sr^{2+} and Gd^{3+} doped magnetite nanoparticles for magnetic hyperthermia and drug delivery application, Ceram. Int., (2023), doi: 10.1016/j.ceramint.2023.03.102.
[56] M. Osial, A. Pregowska, M. Warczak, M. Giersig, Magnetorheological fluids: a concise review of composition, physicochemical properties, and models, J. Intell. Mater. Syst. Struct., (2023), doi: 10.1177/1045389X231157357.
[57] A.S. Teja, P.-Y. Koh, Synthesis, properties, and applications of magnetic iron oxide nanoparticles, Prog. Cryst. Growth Charact. Mater., 55 (2009) 22–45.
[58] J. Tang, M. Su, Q. Wu, L. Wei, N. Wang, E. Xiao, H. Zhang, Y. Wei, Y. Liu, C. Ekberg, B.-M. Steenari, T. Xiao, Highly efficient recovery and clean-up of four heavy metals from MSWI fly ash by integrating leaching, selective extraction and adsorption, J. Cleaner Prod., 234 (2019) 139–149.
[59] A. Sebastian, A. Nangia, M.N.V. Prasad, A green synthetic route to phenolics fabricated magnetite nanoparticles from coconut husk extract: implications to treat metal contaminated water and heavy metal stress in *Oryza sativa* L., J. Cleaner Prod., 174 (2018) 355–366.
[60] J. Hu, G. Chen, I.M.C. Lo, Removal and recovery of Cr(VI) from wastewater by maghemite nanoparticles, Water Res., 39 (2005) 4528–4536.
[61] N.H.Z. Abidin, N.S. Sambudi, N.A. Kamal, Composite of hydroxyapatite-Fe_3O_4 for the adsorption of Methylene blue, ASEAN J. Chem. Eng., 20 (2020) 140, doi: 10.22146/ajche.55015.
[62] A. Vahdat, B. Ghasemi, M. Yousefpour, Synthesis of hydroxyapatite and hydroxyapatite/Fe_3O_4 nanocomposite for removal of heavy metals, Environ. Nanotechnol. Monit. Manage., 12 (2019) 100233, doi: 10.1016/j.enmm.2019.100233.
[63] H.V.T. Luong, N.H. Nguyen, G.H. Khuu, Y.P. Bui, Q.Q.V. Thieu, T.N.M. Ngo, T.B.Q. Tran, Preparation of Fe_3O_4/HAp nanoparticles from eggshells with highly adsorption capacity for Methylene blue, Can Tho Univ. J. Sci., 14 (2022) 18–27.
[64] A. Dâas, O. Hamdaoui, Extraction of anionic dye from aqueous solutions by emulsion liquid membrane, J. Hazard. Mater., 178 (2010) 973–981.
[65] H. Tanaka, E. Tsuda, H. Nishikawa, M. Fuji, FT-IR studies of adsorption and photocatalytic decomposition under UV irradiation of dimethyl sulfide on calcium hydroxyapatite, Adv. Powder Technol., 23 (2012) 115–119.
[66] S. Iconaru, M. Motelica-Heino, R. Guegan, M. Beuran, A. Costescu, D. Predoi, Adsorption of Pb(II) ions onto hydroxyapatite nanopowders in aqueous solutions, Materials, 11 (2018) 2204, doi: 10.3390/ma11112204.
[67] V.T. Hanh, P.T. Nam, N.T. Phuong, D.T.M. Thanh, Electrodeposition of co-doped hydroxyapatite coating on 316L stainless steel, Vietnam J. Sci. Technol., 56 (2018) 94, doi: 10.15625/2525-2518/56/1/10030.

[68] J. Kim, N.S. Sambudi, K. Cho, Removal of Sr^{2+} using high-surface-area hydroxyapatite synthesized by non-additive in-situ precipitation, J. Environ. Manage., 231 (2019) 788–794.
[69] O.V. Alekseeva, A.N. Rodionova, N.A. Bagrovskaya, A.V. Agafonov, Synthesis, structure, and properties of a bentonite–magnetite composite, Prot. Met. Phys. Chem. Surf., 52 (2016) 819–824.
[70] A.A. Alqadami, M.A. Khan, M. Otero, M.R. Siddiqui, B.-H. Jeon, K.M. Batoo, A magnetic nanocomposite produced from camel bones for an efficient adsorption of toxic metals from water, J. Cleaner Prod., 178 (2018) 293–304.
[71] M. Osial, M. Nowicki, E. Klejman, L. Frąś, Investigation of the well-dispersed magnetorheological oil-based suspension with superparamagnetic nanoparticles using modified split Hopkinson pressure bar, Rheol. Acta, 61 (2022) 111–122.
[72] S. Dagdelen, M. Mackiewicz, M. Osial, E. Waleka-Bargiel, J. Romanski, P. Krysinski, M. Karbarz, Redox-responsive degradable microgel modified with superparamagnetic nanoparticles exhibiting controlled, hyperthermia-enhanced drug release, J. Mater. Sci., 58 (2023) 4094–4114.
[73] P. Pietrzyk, N.T. Phuong, S.J. Olusegun, N.H. Nam, D.T.M. Thanh, M. Giersig, P. Krysiński, M. Osial, Titan yellow and Congo red removal with superparamagnetic iron-oxide-based nanoparticles doped with zinc, Magnetochemistry, 8 (2022) 91, doi: 10.3390/magnetochemistry8080091.
[74] D.T.M. Thanh, N.T. Phuong, D.T. Hai, H.N. Giang, N.T. Thom, P.T. Nam, N.T. Dung, M. Giersig, M. Osial, Influence of experimental conditions during synthesis on the physicochemical properties of the SPION/hydroxyapatite nanocomposite for magnetic hyperthermia application, Magnetochemistry, 8 (2022) 90, doi: 10.3390/magnetochemistry8080090.
[75] Z. Ma, Y. Guan, H. Liu, Synthesis and characterization of micron-sized monodisperse superparamagnetic polymer particles with amino groups, J. Polym. Sci. Polym. Symp., 43 (2005) 3433–3439.
[76] P. Pietrzyk, E.I. Borowska, P. Hejduk, B.C. Camargo, M. Warczak, T.P. Nguyen, A. Pregowska, M. Gniadek, J. Szczytko, S. Wilczewski, M. Osial, Green composites based on volcanic red algae Cyanidiales, cellulose, and coffee waste biomass modified with magnetic nanoparticles for the removal of Methylene blue, Environ. Sci. Pollut. Res., (2023), doi: 10.1007/s11356-023-26425-3.
[77] M. Mercurio, S. Olusegun, K. Malinska, K. Wystalska, J. Sobik-Szołtysek, A. Dąbrowska, P. Krysiński, M. Osial, Removal of tetracycline and rhodamine from aqueous systems by pristine biochar derived from poultry manure, Desal. Water Treat., 288 (2023) 72–86.
[78] S. Hamidzadeh, M. Torabbeigi, S.J. Shahtaheri, Removal of crystal violet from water by magnetically modified activated carbon and nanomagnetic iron oxide, J. Environ. Health Sci. Eng., 13 (2015) 8, doi: 10.1186/s40201-015-0156-4.
[79] C. Lei, X. Zhu, B. Zhu, J. Yu, W. Ho, Hierarchical NiO–SiO_2 composite hollow microspheres with enhanced adsorption affinity towards Congo red in water, J. Colloid Interface Sci., 466 (2016) 238–246.
[80] H. Zhao, Y. Lang, Adsorption behaviors and mechanisms of florfenicol by magnetic functionalized biochar and reed biochar, J. Taiwan Inst. Chem. Eng., 88 (2018) 152–160.
[81] V.S. Munagapati, V. Yarramuthi, Y. Kim, K.M. Lee, D.-S. Kim, Removal of anionic dyes (Reactive black 5 and Congo red) from aqueous solutions using banana peel powder as an adsorbent, Ecotoxicol. Environ. Saf., 148 (2018) 601–607.
[82] H.-Y. Zhu, Y.-Q. Fu, R. Jiang, J.-H. Jiang, L. Xiao, G.-M. Zeng, S.-L. Zhao, Y. Wang, Adsorption removal of Congo red onto magnetic cellulose/Fe_3O_4/activated carbon composite: Equilibrium, kinetic and thermodynamic studies, Chem. Eng. J., 173 (2011) 494–502.
[83] N.T. Phuong, N.T. Thom, P.T. Nam, N.V. Trang, T.T.T. Huong, D.T. Hai, L.P. Thu, M. Osial, D.T.M. Thanh, Co^{2+} and Cr^{3+} ions removal from wastewater by using nanostructural hydroxyapatite, Vietnam J. Chem., 60 (2022) 135–147.
[84] S.J. Olusegun, M. Osial, T.G.F. Souza, M. Krajewski, G.L.S. Rodrigues, P. Marek, P. Krysinski, Comparative characteristics and enhanced removal of tetracycline and ceftriaxone by Fe_3O_4-lignin and Fe_3O_4-carbon-based lignin: mechanism, thermodynamic evaluation, and DFT calculation, J. Mol. Liq., 371 (2023) 121075, doi: 10.1016/j.molliq.2022.121075.
[85] K. Litefti, M.S. Freire, M. Stitou, J. González-Álvarez, Adsorption of an anionic dye (Congo red) from aqueous solutions by pine bark, Sci. Rep., 9 (2019) 16530, doi: 10.1038/s41598-019-53046-z.
[86] M. Harja, N. Lupu, H. Chiriac, D.-D. Herea, G. Buema, Studies on the removal of Congo red dye by an adsorbent based on fly-ash@Fe_3O_4 mixture, Magnetochemistry, 8 (2022) 125, doi: 10.3390/magnetochemistry8100125.
[87] M.L.D. Bhatlu, P.S. Athira, N. Jayan, D. Barik, M.S. Dennison, Preparation of breadfruit leaf biochar for the application of Congo red dye removal from aqueous solution and optimization of factors by RSM-BBD, Adsorpt. Sci. Technol., 2023 (2023) e7369027, doi: 10.1155/2023/7369027.
[88] Y. Xu, J. Jin, X. Li, Y. Han, H. Meng, T. Wang, X. Zhang, Fabrication of hybrid magnetic HKUST-1 and its high efficient adsorption performance for Congo red dye, RSC Adv., 5 (2015), doi: 10.1039/C5RA00384A.
[89] S. Jana, S.S. Pradhan, T. Tripathy, Poly(N,N-dimethylacrylamide-co-acrylamide) grafted hydroxyethyl cellulose hydrogel: a useful Congo red dye remover, J. Polym. Environ., 26 (2018) 2730–2747.
[90] M.A. Adebayo, J.M. Jabar, J.S. Amoko, E.O. Openiyi, O.O. Shodiya, Coconut husk-raw clay-Fe composite: preparation, characteristics and mechanisms of Congo red adsorption, Sci. Rep., 12 (2022) 14370, doi: 10.1038/s41598-022-18763-y.
[91] R. Lafi, I. Montasser, H. Amor, Adsorption of Congo red dye from aqueous solutions by prepared activated carbon with oxygen-containing functional groups and its regeneration, Adsorpt. Sci. Technol., 37 (2018) 026361741881922, doi: 10.1177/0263617418819227.
[92] S. He, X. Liu, P. Yan, A. Wang, J. Su, X. Su, Preparation of gemini surfactant/graphene oxide composites and their superior performance for Congo red adsorption, RSC Adv., 9 (2019) 4908–4916.
[93] N.E. Messaoudi, M.E. Khomri, N. Chlif, Z.G. Chegini, A. Dbik, S. Bentahar, A. Lacherai, Desorption of Congo red from dye-loaded *Phoenix dactylifera* date stones and *Ziziphus lotus* jujube shells, Groundwater Sustainable Dev., 12 (2021) 100552, doi: 10.1016/j.gsd.2021.100552.
[94] N. Ghosh, S. Sen, G. Biswas, A. Saxena, P.K. Haldar, Adsorption and desorption study of reusable magnetic iron oxide nanoparticles modified with *Justicia adhatoda* leaf extract for the removal of textile dye and antibiotic, Water Air Soil Pollut., 234 (2023) 202, doi: 10.1007/s11270-023-06217-8.
[95] G. Sarojini, S.V. Babu, M. Rajasimman, Adsorptive potential of iron oxide-based nanocomposite for the sequestration of Congo red from aqueous solution, Chemosphere, 287 (2022) 132371, doi: 10.1016/j.chemosphere.2021.132371.
[96] Q. Deng, Q. Luo, M. Li, J. Tu, L. Guo, L. Wu, T. Zhang, L. Shi, H. Zhang, F. Dong, Highly efficient removal of Congo red from aqueous solution by lime-preconditioned phosphogypsum, ChemistrySelect, 7 (2022) e202200139, doi: 10.1002/slct.202200139.